

Resolving Atomic Ordering Differences in Group 11 Nanosized Metals and Binary Alloy Catalysts by Resonant High-Energy X-ray Diffraction and Computer Simulations

Valeri Petkov,^{*,†} Sarvjit Shastri,[‡] Shiyao Shan,[§] Pharrah Joseph,[§] Jin Luo,[§] Chuan-Jian Zhong,[§] Takahiro Nakamura,^{||} Yuliati Herbani,[⊥] and Shunichi Sato^{||}

[†]Department of Physics, Central Michigan University, Mt. Pleasant, Michigan 48859, United States

[‡]Advanced Photon Source, Argonne National Laboratory, Argonne, Illinois 60439, United States

[§]Department of Chemistry, State University of New York at Binghamton, Binghamton, New York 13902, United States

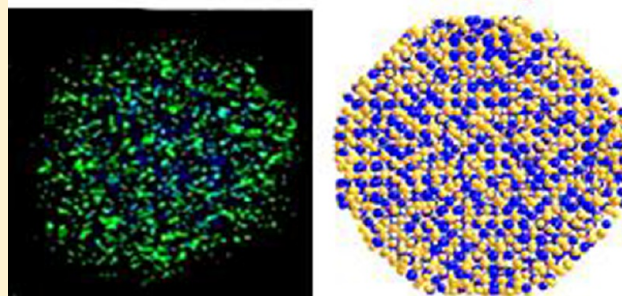
^{||}Institute of Multidisciplinary Research for Advanced Materials, Tohoku University, Katahira 2-1-1, Aoba-ku, Sendai 980-8577, Japan

[⊥]Research Center for Physics, Indonesian Institute of Science, Kawasan Puspiptek Serpong Gedung 440, Jl. Raya Puspiptek, Serpong, Tangerang Banten 15314, Indonesia

S Supporting Information

ABSTRACT: Resonant high-energy X-ray diffraction coupled to atomic pair distribution function analysis and computer simulations is used to study the atomic-scale structure of group 11 nanosized metals and binary alloy catalysts. We find that nanosized Cu is quite disordered structurally whereas nanosized Ag and especially Au exhibit a very good degree of crystallinity. We resolve Cu–Cu and Ag–Ag atomic correlations from Au-involving ones in Au–Cu and Au–Ag nanoalloys and show that depending on the synthetic route group 11 binary alloys may adopt structural states that obey or markedly violate Vegard's law. In the latter case, Cu and Ag atoms undergo substantial size expansion and contraction by as much as 0.3 and 0.03 Å, respectively, while heavier Au atoms remain practically intact. The size change of Cu and Ag atoms does not follow Pauling's rule of electronegativity predicting charge flow toward the more electronegative Au but occurs in a way such that Cu/Au and Ag/Au atomic size ratios in the nanoalloys become closer to one. Atomic size adjusting and the concurrent charge redistribution result in a synergistic effect of oxygen inactive Au and oxygen very active Cu and Ag leading to nanoalloys with very good activity for low-temperature oxidation of CO.

Random AuCu nanoalloy



1. INTRODUCTION

Progress in nanotechnology requires controlling nanostructure and, hence, properties. However, synthesizing nanostructures by design is still not a trivial task since the outcome of the synthesis effort depends on both kinetic and thermodynamic factors. That is why it is important to be able to determine the outcome of a particular synthesis, i.e., the atomic-scale structure of nanosized materials, in very good detail. Success in this field depends on advancing analytical techniques for structure determination of materials confined to nanoscale dimensions. Here we demonstrate such a technique based on resonant high-energy (~80 keV) X-ray diffraction (XRD) coupled to atomic pair distribution function (PDF) analysis and computer simulations. We apply the technique to nanosized group 11 metals (Cu, Ag, and Au) and alloys (Cu–Au and Ag–Au) which have generated considerable interest because of their very promising optical,¹ magnetic,² biomedical,³ and catalytic properties.^{4–6} Two types of alloys are considered: one obtained by soft chemistry and suspended in hexane and another one

that has been postsynthesis thermally processed and supported on carbon. We find clear structural differences between nanosized Cu, Ag, and Au metals. That is, nanosized Cu is quite disordered structurally whereas nanosized Ag and especially Au exhibit a very good degree of crystallinity, most likely due to electronic structure effects.⁷ We also find clear structural differences between the postsynthesis thermally treated and not treated nanoalloys. In particular, we find that thermally treated Au–Cu and Au–Ag alloys experience very pronounced tensile and compressive stress, respectively. The stress is due to expansion and contraction of Cu and Ag atomic species, respectively, leading to a notable deviation from the so-called Vegard's law. On the other hand, Au–Ag alloys obtained by soft chemistry appear to be kinetically trapped in a solid solution structural state that obeys Vegard's law. Furthermore,

Received: August 10, 2013

Revised: September 24, 2013

Published: September 26, 2013

by probing the K edge of Au, Au-differential, Cu–Cu, and Ag–Ag partial PDFs are obtained for the thermally processed Au–Cu and Au–Ag nanoalloys, respectively. Thanks to the ability of resonant high-energy XRD⁸ to differentiate Ag–Ag and Cu–Cu from Au-involving atomic correlations, the degree of chemical ordering in the thermally processed alloys has been determined. This is not a trivial result since in the case of Au–Ag alloys the difference between Ag–Ag and Au-involving atomic correlations is as small as 0.03 Å. Not surprisingly, the different degree of chemical ordering and stress impact the nanoalloy physicochemical properties, in particular the catalytic ones. We show that mixing oxygen inactive Au with oxygen very active Ag and Cu results in nanoalloys showing very good catalytic properties for low-*T* oxidation of CO. From all studied nanoalloys chemically ordered Au–Cu with higher Cu content (e.g., Au₁₈Cu₈₂) exhibits best catalytic activity. Here we would like to emphasize that the new nanostructure knowledge presented here was possible to be obtained only because of the recent development of high-energy synchrotron radiation sources and synchrotron radiation instrumentation^{9,10} as well as of computational procedures for modeling the three-dimensional (3D) structure of finite size nanoparticles (NP)s.¹¹ This is a very promising analytical approach, opening a new window into the structure of nanosized metals and alloys that are currently produced in rapidly increasing numbers and explored for various applications.

2. EXPERIMENTAL SECTION

A. Synthesis of Au–Cu and Au–Ag Nanoparticles by a Two-Phase Modified Method. The synthesis of AuCu nanoparticles followed a modified two-phase reduction method.¹² Briefly, CuCl₂ and KAuCl₄ were dissolved in water in a controlled ratio. With the presence of a sufficient amount of KBr, Cu²⁺ was converted to CuBr₄²⁻, which was transferred from an aqueous phase to an organic phase by adding a solution of tetraoctylammonium bromide (TOABr) in toluene. After 20 min of vigorous stirring, the aqueous solution was removed. The toluene solution was stirred under argon purge to eliminate all oxygen from the system. Decanethiol (DT) was added, and the solution was stirred for another 1 h. NaBH₄ solution was added dropwise. The solution was stirred for 4 h. The resulting DT-encapsulated AuCu nanoparticles in toluene were collected by removing the solvent and cleaned using ethanol.

The synthesis of AuAg nanoparticles also followed a modified two-phase reduction method.¹³ Briefly, AgNO₃ and KAuCl₄ were dissolved in water in a controlled ratio. With the presence of a sufficient amount of KBr, Ag⁺ was converted to AgBr₂⁻, which was transferred from an aqueous phase to an organic phase by adding a solution of TOABr in toluene. After 30 min of vigorous stirring, the aqueous solution was removed. The toluene solution was stirred under argon purge to eliminate all oxygen from the system. Decanethiol was added, and the solution was stirred for another 1 h. NaBH₄ solution was added dropwise. The solution was stirred for 4 h. The resulting DT-encapsulated AuAg nanoparticles in toluene were collected by removing the solvent and cleaned using ethanol. The nanoparticle product was dissolved in hexane. The nanoparticle composition was cross-checked by inductively coupled plasma–optical emission spectroscopy (ICP-OES). For the measurements, the NP samples were dissolved in aqua regia and then diluted to concentrations in the range of 1–50 ppm. Calibration curves were made from dissolved standards in

the same acid matrix as the unknowns. Standards and unknowns were analyzed 10 times each, resulting in $\pm 2\%$ error. The nanoparticles chemical composition was found to be the Au₇₁Cu₂₉, Au₄₆Cu₅₄, Au₁₈Cu₈₂, Au₇₈Ag₂₂, Au₄₃Ag₅₇, and Au₂₇Ag₇₃.

B. Synthesis of Au–Ag Nanoparticles by High-Energy Laser Irradiation. Aqueous solutions of Au and Ag ions were prepared separately using deionized water at the concentration of 10⁻³ M. Phase transfer of metallic ions from an aqueous to a hexane phase was done by mixing the metal aqueous solution with ethanol containing dodecylamine. After rigorous stirring, hexane was added and the stirring continued. The hexane phase containing metal ions separated quickly from the aqueous phase. The hexane solutions of Au and Ag ions were used as they are or mixed each other in different molar ratios prior to laser irradiation. In the laser radiation experiment, 3 mL of the solutions was introduced in quartz cuvettes and irradiated for several minutes by highly intense femtosecond laser pulses with a wavelength of 800 nm. The intensity of the laser beam at the focal point in the solution was about 10¹⁴ W/cm². The irradiated solutions were washed three times with ethanol to eliminate the excess of dodecylamine. The resulted nanoparticles were dispersed in hexane for further investigation. The nanoparticle's composition was checked by direct current plasma-atomic emission spectroscopy and found to be Au, Ag, Au₇₅Ag₂₅, Au₅₀Ag₅₀, and Au₂₅Ag₇₅. More details of the preparation procedure can be found in ref 14.

C. Catalysts Preparation and Characterization. Au–Ag nanoparticles prepared by high-energy laser irradiation were subjected to high-energy XRD experiments as obtained and stored in hexane solution. On the other hand, Au–Cu and Au–Ag nanoparticles obtained by the two-phase modified method were further processed, including depositing on carbon black and thermal treatment strictly following protocols used for preparing of nanosized catalysts. Briefly, carbon black was suspended in hexane. After sonicating for ~3 h, controlled amounts of Au–Cu and Au–Ag nanoparticles were added into the suspension. The suspension was sonicated for 5 min followed by stirring for ~15 h. The powder was collected and dried under N₂. The thermal treatment involved removal of the nanoparticle organic shells and annealing. The annealing was done in a quartz tube furnace. It consisted of heating at 260 °C in 15% O₂–85% N₂ for 30 min for removing the organic shells and then treating at 400 °C in 15% H₂–85% N₂ atmosphere for 120 min.

The catalytic activity of the Cu–Au and Au–Ag nanoalloy catalysts for CO (1 vol % balanced by N₂) + O₂ (20 vol % balanced by N₂) reaction was measured using a customer-built system including a temperature-controlled reactor, gas flow/mixing/injection controllers, an online gas chromatograph (Shimadzu GC 8A) equipped with 5A molecular sieve, Porapak Q packed columns, and a thermal conductivity detector. The catalytic activity for CO oxidation was determined by analyzing the composition of the tail gas effusing from the quartz microreactor packed with catalyst fixed bed.

D. TEM Characterization. The size and morphology of nanoparticles (NP)s were determined by transmission electron microscopy (TEM). For the TEM measurements NP samples were diluted in hexane and drop cast onto a carbon-coated copper grids followed by solvent evaporation in air at room temperature. TEM work was done at the Center for Advanced Microscopy, Michigan State University, using a JEM-2200FS microscope operated at 200 kV. The microscope is fitted with

an ultrahigh-resolution (UHR) pole piece with a point resolution of 0.19 nm. The energy-dispersive analytical work was done with an attached Oxford INCA system with energy resolution of 140 eV. The images were collected with Gatan Multiscan camera with 1024 × 1024 resolution. Exemplary TEM and HR-TEM images are shown in Figures S1–S3 of the Supporting Information. The average size of the thermally treated particles was found to be 5.0(5) nm while that of the untreated particles was between 2.5(5) nm (pure Au and Ag metals) and 3.5(5) nm (Au–Ag alloys).

E. Synchrotron X-ray Diffraction Experiments and Atomic PDFs Derivation. The experiments were carried out at the 1-ID beamline of the Advanced Photon Source at the Argonne National Laboratory. All samples were measured with X-rays of energy 80.400 keV, which is 325 eV below the K absorption edge of Au. For the measurements both carbon supported samples and samples dissolved in hexane were put in glass capillaries. The respective XRD patterns are given in Figures 1a, 1b, and 1c for carbon-supported Au–Cu NPs,

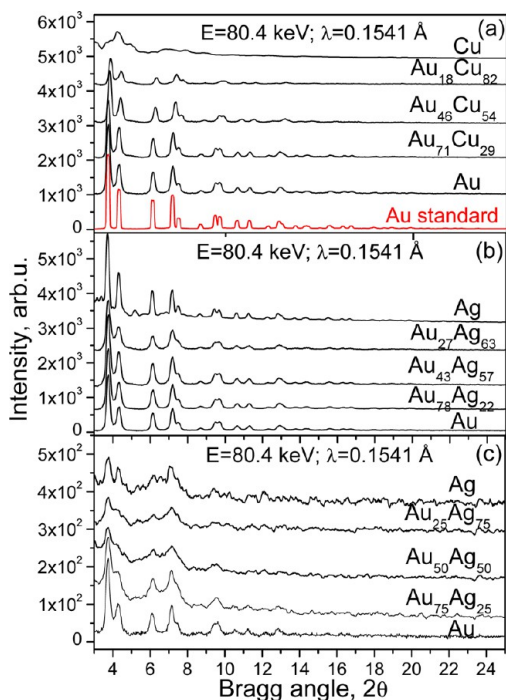


Figure 1. Experimental high-energy XRD patterns for polycrystalline Au standard and Cu, Au, Ag, Cu–Au, and Ag–Au NPs. The data sets are shifted by a constant factor for clarity. Data sets shown in (a) and (b) are for thermally treated particles while that in (c) for hexane suspended particles.

carbon-supported Au–Ag NPs, and Au–Ag NPs in hexane, respectively. Note the high-energy XRD patterns and their Fourier counterparts, the atomic PDFs, considered below reflect assembly averaged structural features of all NPs sampled by the X-ray beam in a way traditional powder XRD represents an assembly average of all polycrystallites sampled by the X-ray beam in those experiments. Comparing particle’s assembly averaged structure features to particle’s assembly averaged properties (e.g., catalytic) puts structure–property relationship exploration on the same footing. In addition, the carbon supported Au₇₁Cu₂₉, Au₄₆Cu₅₄, Au₁₈Cu₈₂, Au₇₈Ag₂₂, Au₄₃Ag₅₇, and Au₂₇Ag₇₃ samples were measured with X-rays of energy 80.700 keV, which is 25 eV below the K adsorption edge of Au

(see Figure S4 of the Supporting Information). The beam was delivered by a combination of a bent double-Laue premonochromator, collimating refracting lenses, and a four crystal high-energy resolution ($\Delta E = 8$ eV) monochromator.^{9,10} The monochromator setup was calibrated and occasionally checked during data collection for stability against sub-eV energy drifts using the K absorption edge of a pure Au foil in transmission. Scattered X-rays were collected by a single, intrinsic Ge detector coupled to a multichannel analyzer. A few energy windows, covering several neighboring channels, were set up to obtain counts integrated over specific X-ray energy ranges during the data collection. These energy windows covered: the elastic/coherent intensity only; the elastic, inelastic/incoherent (Compton), and Au K _{β} fluorescence intensities all together; the Au K _{$\alpha 1$} and K _{$\alpha 2$} fluorescence; and the total intensity scattered into the Ge detector. Integrated counts within these ranges were collected several times scanning up to wave vectors of 25 Å⁻¹ and then averaged to improve the statistical accuracy. The integrated range of only elastically scattered X-ray photons with energy of 80.400 keV was further corrected for detector dead time, sample absorption, and background/pure carbon scattering. The so-corrected XRD data were reduced to structure factors defined as

$$S(q) = 1 + [I^{\text{coh}}(q) - \sum c_i |f_i(q)|^2] / \sum c_i |f_i(q)|^2 \quad (1)$$

where c_i and $f_i(q)$ are the atomic concentration and X-ray scattering factor, respectively, for the atomic species of type i . The structure factors were Fourier transformed into atomic PDFs as follows:

$$G(r) = \frac{2}{\pi} \int_{q=0}^{q_{\text{max}}} q [S(q) - 1] \sin(qr) dq \quad (2)$$

where q is the magnitude of the wave vector ($q = 4\pi \sin \theta / \lambda$), 2θ is the angle between the incoming and outgoing X-rays, and λ is the wavelength of the X-rays used.^{15–18} The so-derived atomic PDFs are shown in Figure 2. Usually they are called “total” PDFs in a sense that they reflect all distinct types of interatomic correlations in the material studied. In particular, for a material comprising n atomic species, the total atomic PDF is a weighted sum of $n(n + 1)/2$ partial PDFs, $G(r_{ij})$, i.e.

$$G(r) = \sum_{i,j} w_{ij} G_{ij}(r) \quad (3)$$

where w_{ij} are weighting factors depending on the concentration and scattering power of the particular atomic species as follows:

$$w_{ij} = c_i c_j \langle f_i(Q) f_j(Q) \rangle / [\sum c_i \langle f_i(Q) \rangle^2] \quad (4)$$

Next, only the elastically scattered from the Au₇₁Cu₂₉, Au₄₆Cu₅₄, Au₁₈Cu₈₂, Au₇₈Ag₂₂, Au₄₃Ag₅₇, and Au₂₇Ag₇₃ NPs intensities collected with 80.700 keV X-rays were subtracted out from the elastically scattered intensities collected with 80.400 keV X-rays. The difference intensity is entirely due to the substantial change in the dispersion corrections (see Supporting Information Figure S4) to the atomic scattering factors of the Au species. The difference intensities were used to derive the so-called Au differential structure factors^{19,20}

$$DS(q)_{\text{Au}} = \frac{I^{\text{coh}}(q, E_1) - I^{\text{coh}}(q, E_2) - [\langle f^2(E_1) \rangle - \langle f^2(E_2) \rangle]}{\langle f(E_1) \rangle^2 - \langle f(E_2) \rangle^2} + 1 \quad (5)$$

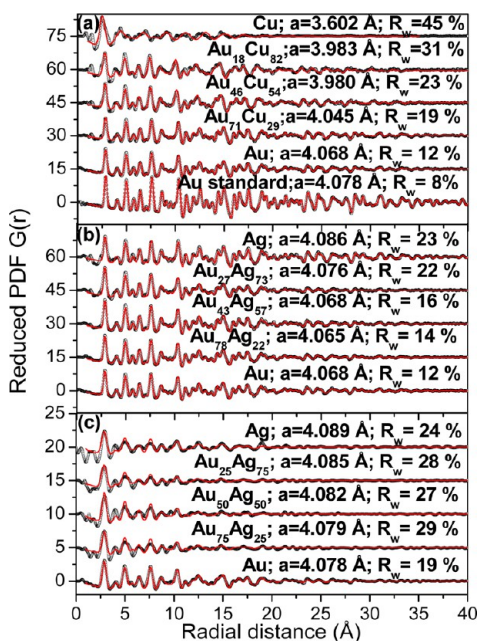


Figure 2. Experimental (symbols) and fcc-model (solid line in red) total atomic PDFs for polycrystalline Au standard and Cu, Au, Ag, Cu–Au, and Ag–Au NPs. The refined fcc lattice parameter and goodness-of-fit factors, R_w , are given by each data set. The data sets are shifted by a constant factor for clarity. Data sets shown in (a) and (b) are for thermally treated particles while that in (c) for hexane suspended particles.

where E_1 and E_2 denote the data sets collected with X-rays of 80.400 and 80.700 keV energy, respectively, and the atomic scattering factors $f(E) = f_0(q) + f'(q, E) + if''(q, E)$ are evaluated with the respective for the two energies dispersion corrections f' and f'' .²⁰ The corresponding Au differential atomic PDFs, $DG(r)_{Au}$, were obtained via a Fourier transformation as follows:

$$DG(r)_{Au} = \frac{2}{\pi} \int_{q=0}^{q_{max}} q [DS(q)_{Au} - 1] \sin(qr) dq \quad (6)$$

where q_{max} extends to 25 \AA^{-1} . Note, since only the scattering form factor of Au atoms changed significantly, the differential atomic PDF contains contributions from atomic pairs involving Au- i type atoms only, i.e.

$$DG(r)_{Au} = \sum_i \Delta w_{Au-i} G_{Au-i}(r) \quad (7)$$

where

$$\Delta w_{Au-i} = \frac{c_{Au} c_i \text{Re}[f_i^*(E_1) - f_i^*(E_2)]}{\langle f(E_1) \rangle^2 - \langle f(E_2) \rangle^2} \quad (8)$$

and $f^*(E)$ is the complex conjugate of $f(q)$ and $i = \text{Au, Ag, or Cu}$, respectively. The Au differential atomic PDFs for Au–Cu and Au–Ag alloy NPs are shown in Figure 4.

Furthermore, by using the recently introduced MIXSCAT approach,²¹ the Cu–Cu and Ag–Ag correlations in Au–Cu and Au–Ag NPs were also obtained from the experimental total PDF and Au differential PDF data. Basically the MIXSCAT approach involves appropriately weighing two experimental atomic PDFs and taking a difference between them to eliminate particular atomic pair correlations that appear in the two PDFs but with different weight contributions.²¹ Following the MIXSCAT approach, the partial Cu–Cu and Ag–Ag atomic

correlations in alloy Au–Cu and Au–Ag NPs were extracted as follows:

$$\begin{aligned} (\text{Cu–Cu/Ag–Ag}) \text{ partial PDF} &= (\text{respective total } G(r)) / w_{ij} \\ &- (\text{respective } DG(r)_{Au}) / \Delta w_{Au-i} \end{aligned} \quad (9)$$

where w_{ij} and Δw_{Au-i} are the weighting factors of the Au–Au and Au–Cu/Ag atomic pairs estimated using the respective definitions given in eqs 4 and 8 above. Note the derivation of the Cu–Cu and Ag–Ag partial PDFs by eq 9 above is relatively straightforward in our case since both experimental PDF data sets involved in it have been derived from XRD data collected on the same instrument with similar statistical accuracy and to the same q_{max} value and also have also been subjected to analogous correction and Fourier transformation protocols. The resulting Cu–Cu and Ag–Ag partial atomic PDFs are shown in Figure 4 introduced later on.

F. Structure Modeling. Bravais lattice constrained fitting of the experimental total PDFs was done with the help of the program PDFgui.²² Data from literature sources²³ for the crystal structures of bulk Au, Ag, and Cu were used as starting values in the fitting. It was done as to minimize a goodness-of-fit indicator, R_w , defined as

$$R_w = \left\{ \frac{\sum w_i (G_i^{\text{exp}} - G_i^{\text{calc}})^2}{\sum w_i (G_i^{\text{exp}})^2} \right\}^{1/2} \quad (10)$$

where G^{exp} and G^{calc} are the experimental and calculated total PDFs, respectively, and w_i are weighting factors reflecting the statistical quality of the individual data points. Results from the fitting are shown in Figure 2. Here it may be noted that the agreement factors achieved with the PDF fits based on lattice-type models are usually in the range of 15–30% as is the case with the present fits. Such R_w 's appear somewhat high when compared to goodness-of-fit factors resulting from Rietveld refinement of XRD data in reciprocal space. This mostly reflects the fact that the atomic PDFs being fit take both the sharp, Bragg-like features and the diffuse component of the XRD data into account while Rietveld fits consider only the former. The inherently higher absolute value of the goodness-of-fit factors in PDFs fits, however, does not affect their functional purpose as a residuals quantity that guides the refinement of the structural parameters of the tested Bravais lattice-based models.

Finite size atomic configurations cut out of a perfect fcc-lattice were used to start the reverse Monte Carlo simulations.²⁴ The configurations were spherical in shape and about 5.0 nm in diameter, i.e., with a size and shape similar to those of the NPs studied here. In the simulations the position of each atom from the approximately 5000 atom configurations was adjusted as to minimize the difference R_w (see eq 10) between the model and experimental total and partial PDF data. Atoms were constrained (i) not to come closer than preselected distances of closest approach and (ii) to maintain as maximal (i.e., as close to 12) as possible coordination numbers. The first constraint reflects the fact that, for example, metal atoms in the NPs studied do not approach each other closer than the sum of the respective atomic radii. The second constraint takes into account the close packing nature of the fcc-type atomic ordering in the metallic NPs studied here. At the same time the energy of the configurations was optimized by minimizing pairwise (Lennard-Jones type) potentials for Au, Ag, and Cu taken from literature sources.²⁵ The simulations were done with the help of a new version of the program RMC++²⁶ expanding

on our recent work published in refs 11 and 27. The reverse Monte Carlo simulations refined structure models for Au–Cu and Au–Ag NPs are shown in Figure 7.

3. RESULTS AND DISCUSSION

Typical for materials of nanosized dimensions, the particles studied here show rather diffuse XRD patterns with broad peaks (see Figure 1), rendering traditional crystallography-based structure analysis hardly applicable. As we^{15–18} and others²⁸ have repeatedly shown, the task is greatly simplified if not the diffuse XRD patterns but their Fourier transforms, the so-called atomic PDFs, are considered instead. In brief, the frequently used atomic PDF $G(r)$ peaks at distances separating pairs of atoms, i.e., where the local atomic density exceeds the average one, while the areas under the PDF peaks are proportional to the number of atomic pairs at those distances. In this respect $G(r)$ resembles the so-called Patterson function that is widely applied in traditional X-ray crystallography.²⁹ However, while the Patterson function peaks at interatomic distances within the unit cell of a crystal, $G(r)$ does not imply any lattice periodicity and so reflects all interatomic distances occurring in the material studied. This is a great advantage when studying finite size materials such as 2–5 nm particles whose structure may not necessarily be well described in terms of infinite periodic lattices used for their bulk counterparts. Experimental atomic PDFs for the NPs studied here are shown in Figure 2. Note thus derived atomic PDFs are usually called total in a sense that they show all distinct types of interatomic correlations in the respective materials. For Cu, Ag, and Au NPs the total PDFs thus reflect the correlations between the only one type of chemical species present: Cu–Cu, Ag–Ag, and Au–Au correlations, respectively. For the binary alloy NPs the total PDFs in Figure 2 reflect the correlations between the two types of chemical species present: those are Cu–Cu, Cu–Au, and Au–Au correlations for the Cu–Au nanoalloys (Figure 2a) and Ag–Ag, Ag–Au and Au–Au correlations for the Ag–Au nanoalloys (Figure 2b,c).

An inspection of the data in Figure 2 shows that all experimental PDFs have well-defined peaks to distances of a few nanometers, reflecting the presence of well-defined local atomic ordering. The peaks decay to zero faster than those in the PDF for a standard Au sample which extends to high interatomic distances as it should be with a polycrystalline material. The real space distance at which the NP PDFs decay to zero is commensurate to the so-called length of structural coherence. With all NPs studied here this length appears shorter than the respective NP size, indicating the presence of substantial structural distortions. Such are typical for NPs and are usually due to finite size and surface relaxation effects.

To gain a better insight into the NPs' atomic-scale structure, we employed two distinct modeling approaches. At first the experimental total PDF data were approached with models based on crystalline lattices. In this type of modeling a PDF for an infinite crystalline lattice is first computed. Then each of the coordination spheres of the perfect lattice is broadened by a convolution with a Gaussian function to take into account the presence of thermal (Debye–Waller type) and static local atomic displacements in NPs. At the same time the computed PDF is multiplied by a particle shape (spherical in our case)-dependent function which is zero for distances longer than the size of the NPs being modeled. It is a simplistic approximation to the structure of real NPs but is useful since it allows (i) to verify the type of their atomic ordering and (ii) to obtain a set

of structural parameters (e.g., lattice parameters) that may be used to distinguish between different NPs. The calculations were done with the help of the program PDFgui.²² Data from literature sources for the face-centered cubic (fcc)-type lattices occurring with group 11 bulk metals and alloys were used as starting values in the NP structure modeling.

As can be seen in Figures 2a and 2b the experimental atomic PDFs for pure Au and Ag NPs are very well approximated by a model featuring a fcc-type atomic arrangement. This model works less well but still acceptable for Ag–Au and Cu–Au alloy NPs. The model performs worst with pure Cu NPs indicating substantial structural disorder as discussed below. The fcc lattice parameters resulted from the fits are shown in Figure 2 and also summarized in Figure 3. As can be seen in the Figure

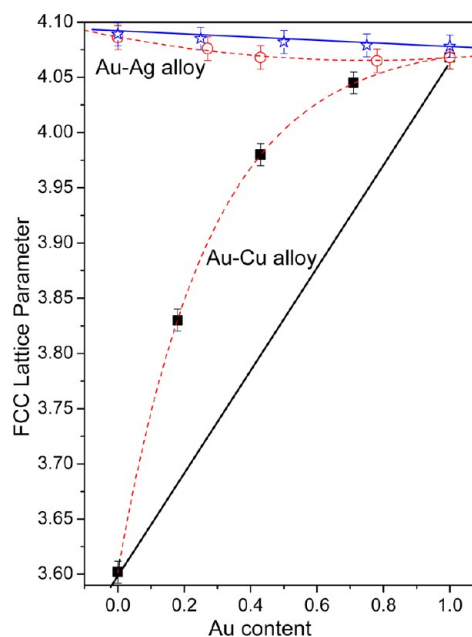


Figure 3. The fcc lattice parameter as a function of Au content in Au–Cu (black squares) and Au–Ag (open circles) nanoalloys that have been thermally processed at 240 °C in an O₂ atmosphere followed by a processing at 400 °C in a H₂ atmosphere. Data for Au–Ag alloys (stars in blue) that have not been postsynthesis treated are shown as well. Broken lines are a guide to the eye. Solid lines follow the predictions of Vegard's law.

2c, the lattice parameters of Au and Ag NPs obtained by a laser assisted wet chemical procedure are close to those of bulk Au and Ag. For reference, the lattice parameters for bulk Ag, Au, and Cu metals are 4.09, 4.07, and 3.61 Å, respectively. Also, the lattice parameter of the wet NPs scales linearly with the Au/Ag ratio strictly obeying the so-called Vegard's law (see Figure 3). The result indicates that as obtained and studied in hexane Au–Ag NPs are a true solid solution of Ag and Au atoms that keep their elemental atomic dimensions of 2.88 and 2.89 Å, respectively, intact when alloyed together. This leads to a gradual increase of the fcc lattice parameter of the nanoalloys with increasing the relative amount of the larger in size Ag atoms (see Figure 3, upper part). The situation is very different with the Au–Ag and Au–Cu NPs that have been postsynthesis treated at elevated temperatures following established protocols for preparing of nanosized catalysts. The concentration dependence of the fcc-lattice parameter for Au–Cu NPs shows a very large positive deviation from the linear

dependence predicted by Vegard's law, indicating that the nanoalloys are under very substantial tensile stress. On the other hand, the concentration dependence of the fcc-lattice parameter for the thermally processed Au–Ag NPs shows a negative deviation from the linear dependence predicted by Vegard's law, indicating that these nanoalloys are under compressive stress. Note a positive deviation from Vegard's law has been observed with bulk Au–Cu alloys and a negative deviation with bulk Au–Ag alloys.^{30–32} In bulk Au–Ag alloys the maximal deviation of the fcc lattice parameter, a , from Vegard's law is found to be $\Delta a = -0.006 \text{ \AA}$.³⁰ It is about $\Delta a = -0.018 \text{ \AA}$ in the case of the thermally treated Au–Ag NPs studied here. In bulk Au–Cu alloys the maximal deviation from Vegard's law has been found to be $\Delta a = +0.05 \text{ \AA}$.²⁸ In the case of thermally processed Au–Cu NPs studied here $\Delta a_{\text{max}} = +0.17 \text{ \AA}$. Here Δa is the difference between the Vegard's law predicted and experimental lattice parameters, a , corresponding to alloy NPs of 1:1 composition. As our results show when confined to nanoscale dimensions Au–Cu and Au–Ag alloys may accommodate tensile and compressive stress, respectively, which is about 3 times larger than that observed in their bulk state.

Vegard's law has been used extensively in mineralogy, metallurgy, and materials science for several decades. According to the law, unit cell parameters should vary linearly with composition for a continuous solid solution in which atoms that substitute for each other keep their dimensions and are randomly distributed. This is what we observe with Ag–Au NPs obtained by a laser assisted wet chemical procedure. Deviations from Vegard's law have been associated with a modification of the electronic structure of the alloyed atomic species.³³ A modification of the electronic structure comes from charge transfer resulting in a change in the dimensions of the alloyed atomic species and, hence, in the respective lattice parameters. For example, as postulated by the theory of chemical bonding of Pauling,^{34,35} metal atoms absorbing an extra electron would become smaller in size due to the increased attraction of the electron cloud by the nuclei while ones losing electron would become larger. Pauling has also proposed that charge transfer on the metallic atom-pair bond on alloying would be proportional to the electronegativity difference between the respective atoms, for maintaining electroneutrality. For reference, the electronegativity of Au is 2.4. It is 1.93 for Ag and 1.9 for Cu, suggesting charge transfer toward Au in the Au–Cu and Au–Ag nanoalloys studied here. In reality, other factors such as minimization of the internal stresses also play an important role in determining the direction and amount of charge transfer upon alloying. For example, it has been shown that the dimensions of free atoms and, hence, their electronic structure change upon alloying so that the ratio of the atomic dimensions of the alloyed atoms becomes as close to one as possible.^{34,36} In our case the modification of the electronic structure of atoms is such that upon introduction of larger Ag ($d_{\text{Ag}} = 2.89 \text{ \AA}$) atoms into a matrix of smaller Au ($d_{\text{Au}} = 2.88 \text{ \AA}$) atoms followed by a thermal treatment leads to shrinking of the lattice parameter of the resulted nanoalloy. The opposite effect is observed with the introduction of smaller Cu ($d_{\text{Cu}} = 2.56 \text{ \AA}$) atoms into a matrix of larger Au atoms. Here the lattice parameter of the resulting nanoalloys increases well beyond the predictions of Vegard's law (see Figure 3).

To understand which of the metallic species in the thermally treated Au–Cu and Au–Ag nanoalloys change their dimensions and what is the chemical type of the resulted

alloys atomic-scale structure data with added chemical specificity is needed. Sensitivity to the chemical type of atomic species may be added by employing imaging techniques such as high-angle annular dark field or energy dispersive spectroscopy coupled scanning transmission electron microscopy (HAADF/EDS-STEM) or other spectroscopic techniques such as extended X-ray absorption fine structure spectroscopy (EXAFS). HAADF/EDS-STEM can reveal compositional variations in NPs with atomic resolution but, like any other images, HAADF/EDS-STEM images are just a projection down an axis and so not very sensitive to the atomic dimensions and ordering inside alloy NPs. Likewise, the EXAFS technique is very useful but yields information on the atomic-scale structure extending out to 5–6 \AA only. Thus, for example, an EXAFS experiment would hardly distinguish between a hexagonal and fcc type of alloy NPs since both show first and second coordination spheres of 12 and 6 atoms, respectively. As we showed recently,⁸ the difficulty can be overcome by employing the so-called resonant high-energy XRD, which involves measuring two diffraction data sets close to but below the absorption edge of an atomic species, taking the difference between these two data sets, and Fourier transforming it into a quantity called a differential atomic PDF. By combining total and differential PDFs, partial atomic PDFs can be extracted as well.⁸ Similarly to EXAFS, the differential and partial PDFs will reflect only interatomic correlations of particular chemistry. However, unlike EXAFS, resonant high-energy XRD will reveal these correlations up to the longest interatomic distances to which they extend. Details of our resonant high-energy XRD experiments are given in the Experimental Section.

Au-differential, Cu–Cu, and Ag–Ag partial atomic PDFs derived by resonant high-energy XRD experiments conducted at the K edge of Au are shown in Figure 4. The partial Cu–Cu

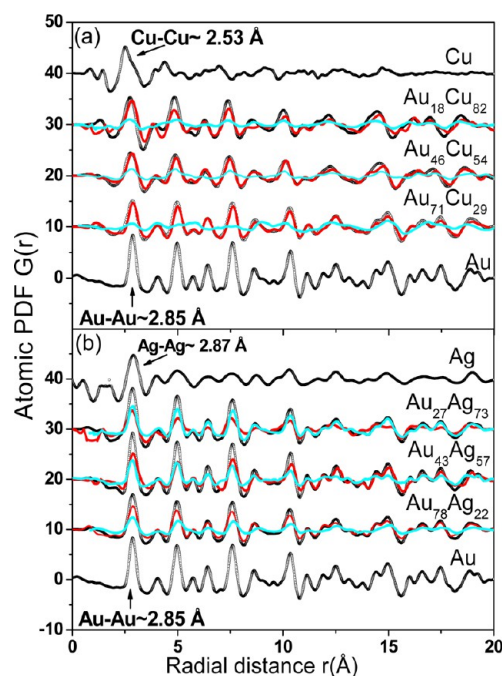


Figure 4. Experimental total atomic PDFs for thermally treated 5 nm Au–Cu and Au–Ag particles (symbols). Experimental Au-differential PDFs (line in red), Cu–Cu (a), and Ag–Ag (b) partial PDFs (line in cyan) are also shown. Arrows mark the positions of first neighbor bond distances. Data sets are shifted by a constant factor for clarity.

PDF (Figure 4a) reflects the correlations between the Cu atomic species across the Au–Cu NPs. Its first peak corresponds to the shortest Cu–Cu distances, i.e., to the dimension of Cu atoms in the respective nanoalloys. The peak is positioned at 2.68 Å in Au₁₈Cu₈₂, 2.78 Å in Au₄₆Cu₅₄, and 2.83 Å in Au₇₁Cu₂₉ alloy. For reference, the first peak in the PDF for pure Cu NPs is positioned at 2.53 Å (see Figure 4a). At the same time the first peak in the Au-differential PDFs hardly changes its position at 2.86 Å. The results show that Cu atoms expand markedly when alloyed with Au. The expansion increases with the relative Au content and amounts to 0.3 Å in the case of Au₇₁Cu₂₉ alloy. The partial Ag–Ag reflects the correlations between the Ag atomic species across the Au–Ag NPs (see Figure 4b). Its first peak corresponds to the shortest Ag–Ag distances, i.e., to the dimension of Ag atoms in the respective nanoalloys. The peak is positioned at 2.86 Å in Au₂₇Ag₇₃, 2.85 Å in Au₄₃Ag₅₇, and 2.84 Å in Au₇₈Ag₂₂ alloys. For reference, the first peak in the PDF for pure Ag NPs is positioned at 2.87 Å and that in the PDF for pure Au NPs—at 2.85 Å. At the same time the first peak in the Au-differential PDFs hardly changes its position at 2.87 Å (see Figure 4b). Results clearly show that Ag atoms contract when alloyed with Au. The contraction increases with the relative Au content and amounts to 0.03 Å in the case of Au₇₈Ag₂₂ alloys. This conclusion would have been very difficult to arrive at if it has not been for high-energy resonant XRD that allows differentiating between Ag- and Au-involving first-neighbor correlations differing in as little as 0.03 Å. Such a fine atomic species resolution is hardly, if at all, possible to achieve by other experimental techniques. The overall picture that emerges from the high-energy XRD experiments and analysis of the experimental PDF data is the following: if group 11 nanosized alloys are not subjected to extra thermal treatment (e.g., the Au–Ag nanoalloys obtained and suspended in hexane), they may end up in a true solid solution structural state where atoms keep their elemental dimensions. Such nanoalloys obey Vegard's law (see Figure 3). Postsynthesis treating of group 11 nanosized alloys at elevated temperatures lets them sample a larger structural space and adopt structures where atomic species adjust their sizes so that a better thermodynamical equilibrium is achieved (e.g., carbon-supported Au–Cu and Au–Ag alloys studied here). Such nanoalloys may markedly violate Vegard's law (see Figure 3). Obviously, by properly choosing the preparation and postsynthesis treatment conditions quite different from a structural point of view, group 11 nanosized alloys can be obtained. This is another demonstration of the “there is plenty of room at the bottom concept”³⁷ of today's nanotechnology.

Revealing how exactly Au, Ag, and Cu metal species are mixed together across the thermally treated NPs requires exploring structural and chemical order/disorder effects going beyond the limits of a unit cell of a fcc lattice. For that purpose we employed reverse Monte Carlo (RMC) simulations guided by the experimental total and partial PDFs data. Contrary to the crystalline lattice-based models, RMC simulations do not imply any structural periodicity and uniformity and so are very suitable to study finite size NPs. 3D models of spherical shape and size (about 5 nm) corresponding to the studied NPs were used. More details of the RMC simulations are given in the Experimental Section. As can be seen in Figures 5a and 5b the RMC constructed models reproduce the experimental total atomic PDFs for carbon-supported Au–Cu and Au–Ag NPs, respectively, very well. As can be seen in Figures 6a and 6b, the

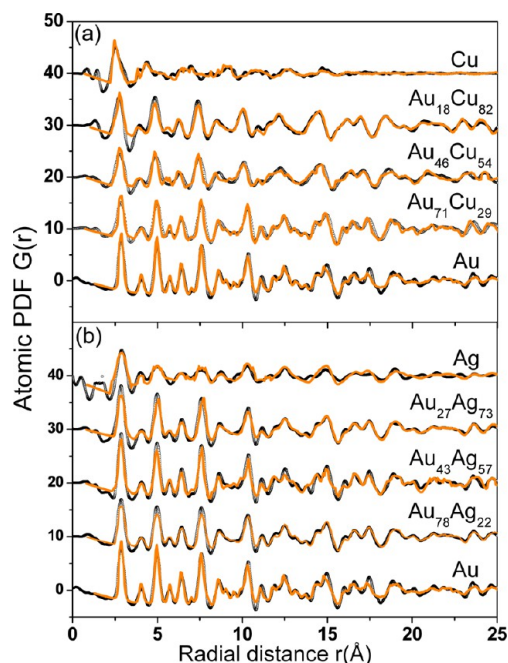


Figure 5. Experimental (symbols) and RMC model (line in red) total atomic PDFs for Au–Cu (a) and Au–Ag (b) thermally treated NPs. The model PDFs are computed from the atomic configurations shown in Figure 7.

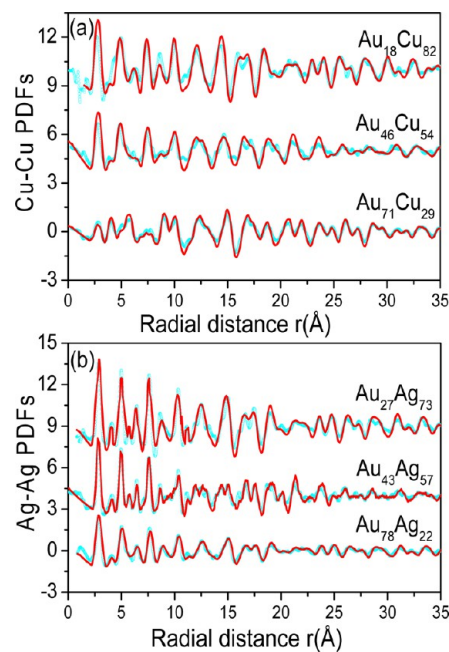


Figure 6. Experimental (symbols in cyan) and RMC model fit (line in red) Cu–Cu (a) and Ag–Ag (b) partial atomic PDFs for Au–Cu and Au–Ag thermally treated nanoalloys, respectively. The model partial PDFs are computed from the atomic configurations shown in Figure 7.

same level of agreement is achieved with the experimental partial atomic PDFs for carbon-supported Au–Cu and Au–Ag NPs, respectively. Snapshots of the RMC constructed structure models are shown in Figure 7.

Inspection of the RMC models for Au, Ag, and Cu 5 nm particles reveals an increasing degree of disorder with diminishing the atomic number, *Z*. In particular, Au NPs appear as a piece of the fcc lattice of bulk Au with very little

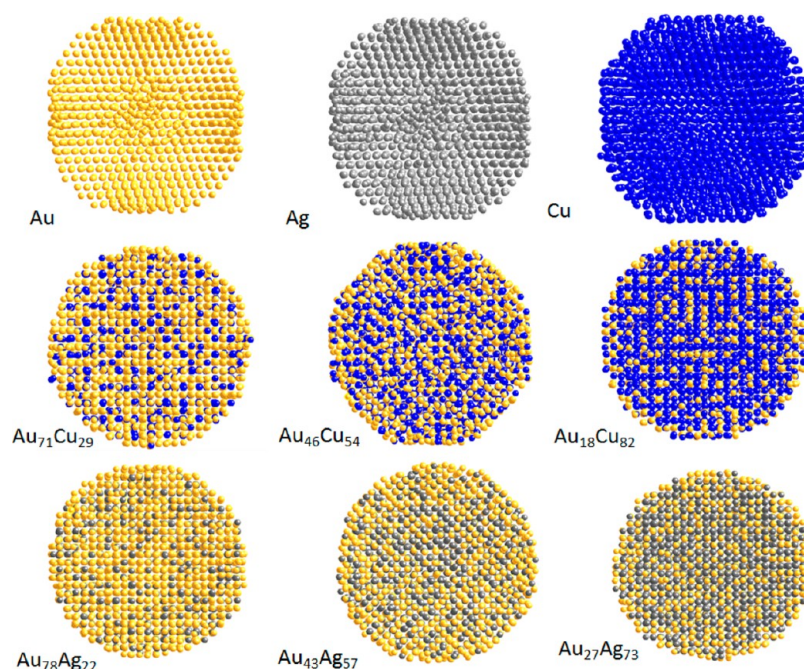


Figure 7. RMC refined atomic configurations (about 5000 atoms each) for thermally treated pure Au, Ag, and Cu metal as well as Au–Cu and Au–Ag alloy NPs. Au atoms are in yellow, Ag atom in gray, and Cu atoms in blue. 3D rendering of the structure models (as animated GIF files) are provided as Supporting Information.

structural disorder. The fcc atomic ordering in Ag NPs seems to suffer a moderate structural disorder. Cu NPs are quite disordered structurally with atoms moved around in an almost uncorrelated manner. This finding of the RMC simulations is in line with the high-resolution TEM data shown in Figure S2 of the Supporting Information. The change of the perfectness of the atomic order in group 11 nanosized metals with the atomic number Z is also well documented by the respective distributions of bond angles computed from the RMC constructed model configurations (see Figure 8). All bond angle distributions presented in the figure cluster around the bond angles for a fcc lattice, indicating that the local atomic ordering in Au, Ag, and Cu NPs studied here is of a fcc type. The scatter of the distributions increases with diminishing the atomic number, Z , and is largest with Cu NPs signaling a substantial degree of local structural disorder. Other studies⁷ have also found that group 11 heavier nanosized metals (e.g., Au and Ag) exhibit a more perfect atomic ordering than lighter ones (e.g., Cu). The effect is related to differences in the electronic structure of the respective elements. The inner electrons of heavier atoms experience larger nuclear charge such that they reach appropriate energy levels needed to achieve a balance with the electrostatic potential. The effect may propagate in such a way that it leads to charge redistribution impacting the use of outer electrons in the chemical bonding. As discussed in ref 7 and references therein, this favors atoms in heavier group 11 nanosized metals occupy sites with a locally higher symmetry, i.e., with a higher degree of structural perfection.

Inspection of the RMC models for $\text{Au}_{71}\text{Cu}_{29}$, $\text{Au}_{46}\text{Cu}_{54}$, $\text{Au}_{18}\text{Cu}_{82}$, $\text{Au}_{78}\text{Ag}_{22}$, $\text{Au}_{43}\text{Ag}_{57}$, and $\text{Au}_{27}\text{Ag}_{73}$ reveals the following structural characteristics of the thermally treated NPs: (i) All alloy NPs show a good degree of crystallinity. High-resolution TEM data shown in Figure S2 support this observation. (ii) All NPs show a good degree of chemical alloying as well. No signatures of cluster-over-cluster, onion-

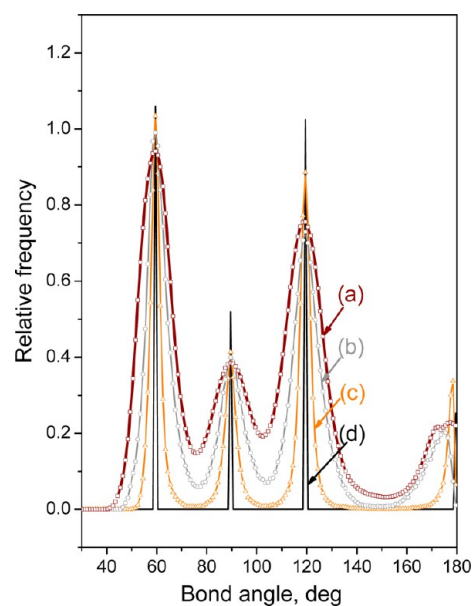


Figure 8. Bond angles distribution in crystalline fcc lattice (curve d; thin solid line in black), 5 nm Au (curve c; up triangles in orange), Ag (curve b; circles in gray), and Cu (curve a; rectangles in wine) thermally treated NPs. Bond angle distributions for the NPs are computed from the respective model configurations in Figure 7.

type, or core–shell morphologies are observed. This result is supported by EDS spectroscopy data shown in Figures 9 and 10. Obviously treating the NPs at elevated temperatures has promoted³⁸ the interdiffusion of metal species, resulting in an alloy-type morphology. (iii) The NPs are not exactly random alloys since some preference of the atomic species to organize in a particular way are observed with the different nanoalloys. For example, Cu atoms in $\text{Au}_{18}\text{Cu}_{82}$ NPs show a tendency to occupy linear chain-type positions (see Figure 7). To quantify

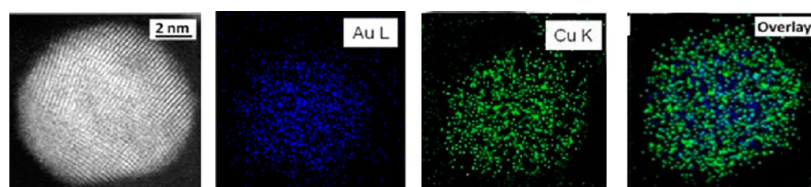


Figure 9. TEM (the most left) and EDS images for elemental mapping of a carbon supported $\text{Au}_{40}\text{Cu}_{60}$ NP. The random distribution of Au and Cu species in the EDS overlay is indicative of a good degree of alloying. Adapted with permission from ref 12. Copyright 2012 American Chemical Society.

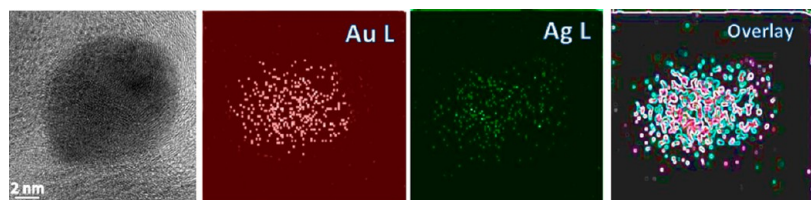


Figure 10. TEM (the most left) and EDS images for elemental mapping of a carbon supported $\text{Au}_{43}\text{Ag}_{57}$ NP. The random distribution of Au and Ag species in the EDS overlay is indicative of a good degree of alloying.

the exact degree of alloying in the thermally treated Au–Cu and Au–Ag NPs studied here, we computed the so-called Cowley's short-range order parameter:^{39,40}

$$\alpha = 1 - \frac{N_{AB}/N_{AT}}{x_b} \quad (11)$$

where x_b is the molar concentration of atomic species of type B, N_{AB} is the number of atomic species of type B in the first coordination sphere of A-type species, and N_{AT} is the total first coordination number of A-type species. Positive numbers of α indicate a tendency for heterogeneity while negative numbers a tendency for chemical ordering.⁴¹ In computing α , we used the N_{AB} and N_{AT} values derived from the RMC constructed models. $\text{Au}_{71}\text{Cu}_{29}$, $\text{Au}_{46}\text{Cu}_{54}$, and $\text{Au}_{18}\text{Cu}_{82}$ nanoalloys showed α values of 0.1, 0.05, and -0.15 . $\text{Au}_{78}\text{Ag}_{22}$, $\text{Au}_{43}\text{Ag}_{57}$, and $\text{Au}_{27}\text{Ag}_{73}$ nanoalloys showed α values of 0.2, -0.03 , and -0.2 , respectively. The analysis of the short-range order parameter values shows that alloy NPs where the relative amount of Cu and Ag is high exhibit a weak tendency for chemical ordering (small negative values of α) while NPs where the amount of Ag and Cu is small exhibit a weak tendency for chemical heterogeneity (i.e., phase segregation). Au–Ag and Au–Cu NPs that are close to the 1:1 composition are almost a random type of alloys ($\alpha \sim 0$). Note the Au–Ag bulk system is characterized by a chemically disordered solid solution for the whole range of concentrations. Depending on the preparation conditions, the Au–Cu bulk system may be a chemically disordered solid solution or exhibit distinct chemically ordered phases at the canonical compositions of 1:3, 1:1, and 3:1. The NPs we study show a somewhat different behavior with a clear tendency for chemical ordering at higher concentrations of the lighter Cu and Ag atomic species and for heterogeneity when Cu and Ag become minority species in the nanoalloys.

Determining not only the type of atomic but also of chemical ordering is important since the relative distribution of the chemical species with respect to each other may have a great impact on NP's properties. For example, although Au, Ag, and Cu belong to the same group, they have very different properties with respect to oxygen absorption. As Au binds oxygen very weakly, oxygen activation is generally thought as a rate-limiting step for most oxidation reactions catalyzed by Au

NPs. In contrast, Ag and Cu absorb oxygen very well, and different oxygen species have been identified on Ag and Cu surfaces. The intrinsically different properties of Au on one side and Ag and Cu on the other toward oxygen activation offer a great potential for fine-tuning the catalytic properties for various oxidizing reactions by alloying. Studies have shown that Ag–Au nanoalloys have high catalytic activity for low- T oxidation of CO.^{42–44} Our own catalytic studies¹² show (see Figure 11a) that Au–Cu alloy NPs also have an excellent activity for CO oxidation. Interestingly chemically ordered Au–Cu nanoalloy with higher Cu content ($\text{Au}_{18}\text{Cu}_{82}$) exhibits a somewhat better activity than chemically disordered Au–Cu

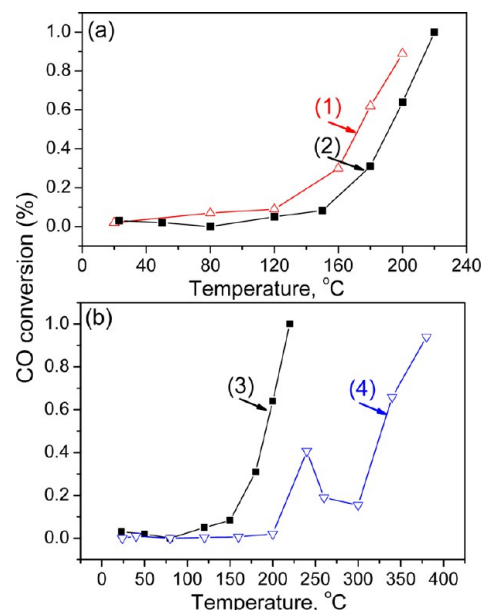


Figure 11. (a) CO conversion for $\text{Au}_{46}\text{Cu}_{54}$ (curve 2; solid squares in black) and $\text{Au}_{18}\text{Cu}_{82}$ (curve 1; up triangles in red) NPs. (b) CO conversion for $\text{Au}_{46}\text{Cu}_{54}$ (curve 3; solid squares in black) and $\text{Au}_{43}\text{Ag}_{57}$ (curve 4; down triangles in blue) NPs. Samples of better catalytic activity are those that exhibit a larger CO conversion at lower temperatures. Note that 100% CO conversion corresponds to 1.0 in the vertical axis of the plot.

nanoalloy ($\text{Au}_{46}\text{Cu}_{54}$) of smaller Cu content. In addition to the synergistic role of Cu atoms in activating oxygen species, this difference may also come from the different arrangement of Cu and Au atoms with respect to each other close and at the surface of the respective nanoalloys (see Figure 7) and/or from the somewhat different level of tensile stress ($\Delta a(\text{Au}_{18}\text{Cu}_{82}) = 0.13 \text{ \AA}$ and $\Delta a(\text{Au}_{46}\text{Cu}_{54}) = 0.16 \text{ \AA}$; see Figure 3) in the different Au–Cu nanoalloys. Furthermore, our data for Au–Cu and Au–Ag nanoalloys of similar Au content (see Figure 11b) show that the former is much more catalytically active for CO conversion than the latter. Besides the different oxophilicity of Cu and Ag, the very strong tensile stress in Au–Cu nanoalloys, as compared to the compressive stress in Au–Ag nanoalloys (see Figure 3), may be behind the better catalytic activity of Au–Cu NPs.

4. CONCLUSION

Advancing science and technology will keep generating nanosized materials with increasingly complex structure and chemistry. The understanding and so getting control over the properties of such materials require precise knowledge of the way atoms are arranged at the nanoscale. High-energy resonant XRD coupled to atomic PDFs analysis and computer simulations can deliver this knowledge with both very good spatial resolution and chemical specificity. To be more specific, our study shows that Cu–Cu and Ag–Ag atomic correlations in 5 nm Au–Cu and Au–Ag particles, respectively, can be clearly revealed and differentiated from Au-involving atomic correlations. Note Ag–Ag and Au-involving first atomic neighbor correlations differ by only about 0.03 Å so the results presented here demonstrate an unprecedented resolving power of chemical species. Our studies also reveal that depending on the preparation conditions group 11 binary alloy NPs may appear as true solid solutions obeying Vegard's law or as alloys showing substantial structural distortions and so markedly violating Vegard's law. In particular, thermally processed Au–Ag NPs experience compressive stress while thermally processed Au–Cu NPs experience tensile stress. The stress is 3 times stronger than that observed with the respective bulk analogues, indicating that Ag and Cu species may contract and expand much stronger when alloyed with Au at the nanoscale. Change in the atomic dimensions of Cu and Ag indicates substantial charge redistribution in the nanoalloys. In our case it does not simply follow Pauling's rule of electronegativity predicting charge flow toward the more electronegative Au but occurs in a way such that Cu/Au and Ag/Au atomic size ratios in the nanoalloys become closer to one. In this process the atomic dimensions of heavier Au stay almost intact. Also, likely due to electronic structure effects, and in line with other studies,⁷ we find that lighter group 11 elements such as Cu and Ag are not only more prone to size change but also more structurally disordered at the nanoscale than heavier group 11 elements such as Au. Yet, like Au, nanosized Ag and Cu possess a fcc-type structure. Three-dimensional structure modeling helps reveal that thermally processed group 11 metals tend to form chemically ordered-type of binary alloys at low concentrations of Au and disordered type of binary alloys when the relative amount of Au is higher than 50%. Atomic size adjusting and the concurring charge redistribution taking place with alloying result in a synergistic effect of oxygen inactive Au and oxygen very active Cu and Ag leading to nanocatalysts with very good activity for low-temperature oxidation of CO, providing another example for the usefulness of alloying at

the nanoscale. As our work demonstrates, nanotechnology synthesis effort outcomes can be very precisely determined by advanced analytical techniques such as high-energy resonant XRD coupled to atomic PDFs analysis and structure modeling, presenting excellent opportunities for NP properties fine-tuning and improvement.

■ ASSOCIATED CONTENT

Supporting Information

TEM images, energy dependence of the real f' and imaginary f'' dispersion corrections for Au, and 3D rendering of the RMC generated structure models (as animated GIF files). This material is available free of charge via the Internet at <http://pubs.acs.org>.

■ AUTHOR INFORMATION

Corresponding Author

*E-mail petko1vg@cmich.edu; Tel +989 774 3395; Fax +989 774 2697 (V.P.).

Notes

The authors declare no competing financial interest.

■ ACKNOWLEDGMENTS

Work on this paper was supported by DOE-BES Grant DE-SC0006877. Work at the Advanced Photon Source was supported by DOE under Contract DEAC02-06CH11357.

■ REFERENCES

- (1) Mulvaney, P. Surface Plasmon Spectroscopy of Nanosized Metal Particles. *Langmuir* **1996**, *12*, 788–800.
- (2) Alloyeau, D.; Ricolleau, C.; Mottet, C.; Oitkawa, T.; Langlois, C.; Le Bouar, Y.; Braidy, N.; Loiseau, A. Size and Shape Effects on the Order–Disorder Phase Transition in CoPt Nanoparticles. *Nat. Mater.* **2009**, *8*, 940–946.
- (3) Lin, Ch.-An. J.; Lee, Ch.-H.; Hsieh, J.-T.; Wang, H. H.; Li, J. K.; Shen, J. L.; Chan, W. H.; Yeh, H.-I.; Chang, W. H. Synthesis of Fluorescent Metallic Nanoclusters toward Biomedical Application. *J. Med. Electron. Biol. Eng.* **2009**, *29*, 276–283.
- (4) Samorjai, G. A. In *Introduction to Surface Chemistry and Catalysis*; Wiley: New York, 1994.
- (5) Enache, D. I.; Edwards, J. K.; Landon, P.; Solsona-Espriu, B.; Carley, A. F.; Herzing, A. A.; Watanabe, M.; Kiely, C. J.; Knight, D. W.; Hutchings, G. J. Solvent-Free Oxidation of Primary Alcohols to Aldehydes Using Au–Pd/TiO₂ Catalysts. *Science* **2006**, *311*, 362–365.
- (6) Norskov, J. K.; Christensen, S. H. Toward Efficient Hydrogen Production at Surfaces. *Science* **2006**, *312*, 1322–1323.
- (7) Sanchez, S. I.; Small, M. W.; Bozin, E. S.; Wen, J.-G.; Zuo, J.-M.; Nuzzo, R. G. Metastability and Structural Polymorphism in Noble Metals: The Role of Composition and Metal Atom Coordination in Mono- and Bimetallic Nanoclusters. *ACS Nano* **2013**, *7*, 1542–1557.
- (8) Petkov, V.; Wanjala, B. N.; Loukrakpam, R.; Luo, J.; Yang, L.; Zhong, C. J.; Shastri, S. Pt–Au Alloying at the Nanoscale. *Nano Lett.* **2012**, *12*, 4289–4299.
- (9) Shastri, S. D.; Fezzaa, K.; Mashayekhi, A.; Lee, W.-K.; Fernandez, P. B.; Lee, P. L. Cryogenically Cooled Bent Double-Laue Monochromator for High-Energy Undulator X-rays (50–200 keV). *J. Synchrotron Radiat.* **2002**, *9*, 317–322.
- (10) Shastri, S. D. Combining Flat Crystals, Bent Crystals and Compound Refractive Lenses for High-Energy X-ray Optics. *J. Synchrotron Radiat.* **2004**, *11*, 150–156.
- (11) Petkov, V.; Moreels, I.; Hens, Z.; Ren, Y. PbSe Quantum Dots: Finite, off-Stoichiometric, and Structurally Distorted. *Phys. Rev. B* **2010**, *81*, 241304.
- (12) Yin, J.; Shan, S.; Yang, L.; Mott, D.; Malis, O.; Petkov, V.; Cai, F.; Ng, M. S.; Luo, J.; Chen, B. H.; Engelhard, M. Gold–Copper

Nanoparticles: Nanostructural Evolution and Bifunctional Catalytic Sites. *Chem. Mater.* **2012**, *24*, 4662–4674.

(13) Kariuki, N. N.; Luo, J.; Maye, M.; Hassan, A.; Menard, T.; Naslund, H. R.; Lin, Y.; Wang, C.; Engelhard, M. H.; Zhong, C. J. Composition-Controlled Synthesis of Bimetallic Gold-Silver Nanoparticles. *Langmuir* **2004**, *20*, 11240–11246.

(14) Herbani, Y.; Nakamura, T.; Sato, S. Synthesis of Near-Monodispersed Au-Ag Nanoalloys by High Intensity Laser Irradiation of Metal Ions in Hexane. *J. Phys. Chem. C* **2011**, *115*, 21592–21598.

(15) Petkov, V. Nanostructure by High-Energy X-ray Diffraction. *Mater. Today* **2008**, *11*, 28–38.

(16) Petkov, V.; Bedford, H.; Knecht, M. R.; Weir, M. G.; Crooks, R. M. Periodicity and Atomic Ordering in Nanoparticles of Crystals. *J. Phys. Chem. C* **2008**, *112*, 8907–8911.

(17) Petkov, V.; Peng, Y.; Williams, G.; Huang, B.; Tomalia, D.; Ren, Y. Structure of Gold Nanoparticles Suspended in Water Studied by X-ray Diffraction and Computer Simulations. *Phys. Rev. B* **2005**, *72*, 195402.

(18) Proffen, Th.; Petkov, V.; Billinge, S. J. L.; Vogt, T. Chemical Short Range Order Obtained from the Atomic Pair Distribution Function. *Z. Kristallogr.* **2002**, *217*, 47–50.

(19) Fuoss, P. H.; Eisenberger, P.; Warburton, W. K.; Bienenstock, A. Application of Differential Anomalous X-Ray Scattering to Structural Studies of Amorphous Materials. *Phys. Rev. Lett.* **1981**, *46*, 1537–1540.

(20) Petkov, V.; Shastri, S. D. Element-Specific Structure of Materials with Intrinsic Disorder by High-Energy Resonant X-ray Diffraction and Differential Atomic Pair-Distribution Functions: A Study of PtPd Nanosized Catalysts. *Phys. Rev. B* **2010**, *81*, 165428.

(21) Wurden, C.; Page, K.; Llobet, L.; White, C. E.; Proffen, Th. Extracting Differential Pair Distribution Functions Using MIXSCAT. *J. Appl. Crystallogr.* **2010**, *43*, 635–638.

(22) Farrow, C. L.; Juhás, P.; Liu, J. W.; Bryndin, D.; E. Božin, S.; Bloch, J.; Proffen, Th.; Billinge, S. J. L. PDFfit2 and PDFgui: Computer Programs for Studying Nanostructure in Crystals. *J. Phys.: Condens. Matter* **2007**, *19*, 335219.

(23) Wyckoff, R. W. G. In *Crystal Structures*, 2nd ed.; Interscience Publishers: New York, 1963.

(24) McGreevy, R. L.; Pusztai, L. A Reverse Monte Carlo Simulation: A New Technique for the Determination of Disordered Structures. *Mol. Simul.* **1998**, *1*, 359–367.

(25) Heinz, H.; Vaia, R. A.; Farmer, B. L.; Naik, R. R. Accurate Simulation of Surfaces and Interfaces of Face-Centered Cubic Metals Using 12–6 and 9–6 Lennard-Jones Potentials. *J. Phys. Chem. C* **2008**, *112*, 17281–17290.

(26) Gereben, O.; Jovari, P.; Temleitner, L.; Pusztai, L. A new Version of the RMC++ Reverse Monte Carlo Programme, Aimed at Investigating the Structure of Covalent Glasses. *J. Optoelectron. Adv. Mater.* **2007**, *9*, 3021–3027.

(27) Welborn, M.; Tang, W.; Ryu, J.; Crooks, R. M.; Petkov, V.; Henkelman, G. A Combined Density Functional and X-ray Diffraction Study of Pt Nanoparticle Structure. *J. Chem. Phys.* **2011**, *135*, 014503.

(28) Egami, T.; Billinge, S. J. L. In *Underneath the Bragg Peaks*; Pergamon Press: Oxford, 2003.

(29) Giacovazzo, G., Ed. In *Fundamentals of X-ray Crystallography*; Oxford University Press: New York, 1998.

(30) Lubarda, V. A. On the Effective Lattice Parameter of Binary Alloys. *Mech. Mater.* **2003**, *35*, 53–68.

(31) Rosenberg, Yu.; Machavariani, V. Sh.; Voronel, A.; Garber, S.; Rubshtein, A.; Frenkel, S. I.; Stern, E. A. Strain Energy Density in the X-ray Powder Diffraction from Mixed Crystals and Alloys. *J. Phys.: Condens. Matter* **2000**, *12*, 8081–8088.

(32) Okamoto, H.; Chakrabarti, D. J.; Laughlin, D. E.; Massalski, T. B. The Au-Cu (Gold-Copper) System. *Bull. Alloy Phase Diagrams* **1987**, *8*, 454–473.

(33) King, H. W. Quantitative Size-Factors for Metallic Solid Solutions. *J. Mater. Sci.* **1966**, *1*, 79–90.

(34) Pauling, L. Factors Determining the Average Atomic Volumes in Intermetallic Compounds. *Proc. Natl. Acad. Sci. U. S. A.* **1987**, *84*, 4754–4756.

(35) Pauling, L. Electron Transfer in Intermetallic Compounds. *Proc. Natl. Acad. Sci. U. S. A.* **1950**, *36*, 533–328. Pauling, L. *The Nature of the Chemical Bond*; Cornell University Press: Ithaca, NY, 1975.

(36) Rajasekharam, T.; Seshubai, V. Charge Transfer on the Metallic Atom-Pair Bond, and the Crystal Structures Adopted by Intermetallic Compounds. *Acta Crystallogr., Sect. A* **2012**, *68*, 156–165.

(37) “There is Plenty of Room at the Bottom Concept” of today’s nanotechnology is credited to the physicist Richard Feynman at an American Physical Society meeting at Caltech on Dec 29, **1959**.

(38) Buffat, Ph.; Borrel, J.-P. Size Effect on the Melting Temperature of Gold Particles. *Phys. Rev. A* **1976**, *13*, 2287–2298.

(39) Cowley, J. M. An Approximate Theory of Order in Alloys. *Phys. Rev.* **1950**, *77*, 669–675.

(40) Cowley, J. M. Short- and Long-Range Order Parameters in Disordered Solid Solutions. *Phys. Rev.* **1960**, *120*, 1648–1657.

(41) Frenkel, A. I.; Wang, Q.; Sanchez, S. I.; Small, M. W.; Nuzzo, R. G. Short Range Order in Bimetallic Nanoalloys: An Extended X-ray Absorption Fine Structure Study. *J. Chem. Phys.* **2013**, *138*, 064202.

(42) Liu, J. H.; Wang, A. Q.; Chi, Y. S.; Lin, H. P.; Mou, C. Y. Synergistic Effect in an Au–Ag Alloy Nanocatalyst: CO Oxidation. *J. Phys. Chem. B* **2005**, *109*, 40.

(43) Wang, A. Q.; Liu, J. H.; Lin, S. D.; Lin, T. S.; Mou, C. J. A Novel Efficient Au–Ag Alloy Catalyst System: Preparation, Activity, and Characterization. *J. Catal.* **2005**, *233*, 186–197.

(44) Chang, C. M.; Cheng, C.; Wei, C. CO Oxidation on Unsupported Au₅₅, Ag₅₅, and Au₂₅Ag₃₀ Nanoclusters. *J. Chem. Phys.* **2008**, *128*, 124710.